Realization of Topological Valley Hall Edge States of Elastic Waves in Phononic Crystals Based on Material Differences

Jiachao Xu,[1,‡] Yuanzhen Zheng,[1,‡] Tingfeng Ma,[1,*] Hui Chen,[1] Bowei Wu,[1] Ji Wang,[1,†] Shuanghuizhi Li,[1] Iren Kuznetsova,[2] Ilya Nedospasov,[2] Jianke Du,[1] Hao Shi,[1] Dudu Chen,[1] and Fei Sun[1]

[1] *School of Mechanical Engineering and Mechanics, Ningbo University, Ningbo 315211, China*
[2] *Institute of Radio Engineering and Electronics of RAS, Moscow 125009, Russia*

(Received 18 January 2022; revised 5 June 2022; accepted 15 February 2023; published 20 March 2023)

In this study, the topological valley Hall edge states of elastic waves in phononic crystals are realized based on material differences. A phononic crystal structure with lantern rings is proposed. The results show that differences in the Young's modulus or density of lantern-ring materials can cause the destruction of the effective spatial inversion symmetry, which causes the valley Hall phase transition; thus, topological edge states emerge at the interface of two domains with topologically dissimilar phases. For valley topological transport, the traditional method to break the spatial inversion symmetry is by changing the dimensional parameters of scatterers in phononic crystals. However, in many cases, the space between scatterers is extremely small, making it difficult to obtain a sufficiently large band gap. Moreover, it is difficult to change the transport path and operating-frequency range of elastic waves after sample fabrication is finished. Here, the above problems are solved by the realization of valley topological transport based on changes to lantern-ring materials. The waveguide path is reconfigurable, that is, it can be altered conveniently, and the operating frequency can be tuned by changing the lantern-ring materials. These factors are very important for the topological transport of elastic waves. Topological valley transport achieved by this method has a good backscattering-suppression ability and obvious robustness to defects. Realization of topological valley Hall edge states by utilizing material differences provides an effective method for obtaining the topological transport of elastic waves, breaking the limitations of those based only on structural parameter changes, and this has good application prospects in elastic wave manipulation and communication.

DOI: 10.1103/PhysRevApplied.19.034062

I. INTRODUCTION

In the last decade, phononic crystals and metamaterials have attracted considerable attention for their ability to control the propagation of acoustic or elastic waves [1–4]. For phononic crystals, unique properties can be realized by adjusting structural parameters, such as sound and vibration suppression [5,6], negative refraction [7,8], acoustic stealth [9], acoustic focusing [10], and directional propagation of elastic waves [11].

Topological insulators, originating from condensed matters, have become advanced technology for the robust control of the propagation of photons [12]. In recent years, the concept of topological insulators has been introduced to phononic crystals [13–17] and metamaterials [18,19]. At the interface between two phononic crystals with topologically dissimilar phases, the topological phase transition can lead to topologically protected gapless edge states inside the bulk-frequency band gap. Due to topological protection, acoustic backscattering can be suppressed effectively and acoustic waves can be transported robustly against defects.

There are mainly three methods to realize topologically protected wave transport. The first approach is an analog of the quantum Hall effect (QHE). Fleury *et al*. proposed a feasible method to break the T symmetry in acoustics, relying on a moving airflow in ring cavities [20]. Based on this principle, several designs of analogs of the QHE in phononic crystals have been reported [21–23]. Another method establishes analogs of the quantum spin Hall effect by constructing pseudospin dipole and quadrupole modes [24], where Dirac cones can be opened by shrinking or expanding the spacing of the units within the supercell. Thus, the topological edge states of wave propagation can be realized. The third method is based on the valley Hall

*matingfeng@nbu.edu.cn
†wangji@nbu.edu.cn
‡J. Xu and Y. Zheng contributed equally to this work.

effect. Recently, the valley Hall effect was introduced into phononic crystals exhibiting valley-dependent topological transport of acoustic waves [22,25,26] and mechanical elastic waves [27–30]. By breaking the spatial inversion symmetry, valley pseudospins can be obtained by opening the original Dirac degeneracy of a phononic crystal. This method can avoid the complexity of modulating the physical properties in time.

For the valley Hall effect, breaking the spatial inversion symmetry is typically realized by changing the structural parameters of phononic crystals [31,32]. However, in many application cases, the space between scatterers is extremely small [33]; thus, variation ranges of the scatterer size and the space between scatterers are limited, which influences the size of the topological band gap obviously. As a result, the frequency range of topological edge states is very limited. Additionally, in typical designs of topological phononic crystals, the sizes of the scatterers and matrix are fixed and the structure is nondetachable [34]. Thus, for topological waveguides based on phononic crystals, only a fixed bandwidth can be realized, which limits changes in the frequency range of the edge states. Here, the realization of topological transport edge states of elastic waves based on material differences is investigated. The structure of a phononic crystal is designed to be detachable. A set of lantern rings are installed in the cylinders on the substrate plate, which forms the scatterers of the phononic crystal. When the materials of the two lantern rings within the unit cell are different, the effective spatial inversion symmetry is expected to be broken, and the Dirac cone is hopefully opened up, which could lead to the formation of topological edge states. Using this method, waveguides based on topological edge states with different frequency bands can be achieved conveniently by using lantern rings made of different materials.

II. MODEL

On the surface of the substrate, pillars are arranged in a honeycomb structure, as shown in Fig. 1(a), where a is the lattice constant and $\overrightarrow{a_1}$ and $\overrightarrow{a_2}$ are lattice vectors. Each hexagonal cylinder is sheathed by a lantern ring through a small interference fitting. The interior of the lantern rings is hexagonal and the exterior is circular. A hexagonal inner boundary is applied to reduce relative sliding between the pillar and lantern ring, improving the stability of the structure. The unit cell of the phononic crystal is represented within the dashed frame in Fig. 1(a), and a three-dimensional diagram is shown in Fig. 1(b). Pillars A and B represent the two atoms of the hexagonal lattice. Aluminum is considered as the material of the substrate and the pillars, and its elastic parameters are as follows: mass density, $\rho = 2700$ kg/m^3; Young's modulus, $E = 70$ GPa; and Poisson's ratio, $\mu = 0.3$. Bronze alloy is selected for the material of the lantern rings

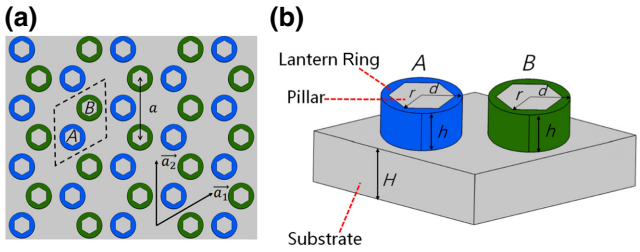

FIG. 1. Schematic diagram of the phononic crystal structure. (a) Phononic crystal plate and (b) unit cell. Bronze alloy is the material of lantern rings (blue) on pillar A, and carbon steel is the material of lantern rings (green) on pillar B.

(blue) on pillar A; its elastic parameters are mass density, $\rho = 8640$ kg/m^3; Young's modulus, $E = 80$ GPa; and Poisson's ratio, $\mu = 0.32$. Carbon steel is selected for the material of the lantern rings (green) on pillar B; its elastic and dimension parameters are as follows: mass density, $\rho = 7900$ kg/m^3; Young's modulus, $E = 185$ GPa; Poisson's ratio, $\mu = 0.325$. The diameters and heights of pillars A and B are identical. The dimension parameters are set as follows: lattice constant $a = 0.008$ m, $r = 0.15a$, $d = 0.22a$, $h = 0.27a$ and $H = 0.35a$. Dispersion-characteristic calculations for the unit cell are performed using the commercial finite-element software COMSOL Multiphysics. Floquet periodic boundary conditions are applied to the unit cell.

Figure 2(a) shows the dispersion characteristics of the unit cell when the lantern rings on pillars A and B are made of the same material (bronze alloy). Due to the C_{6v} symmetry of the structure, a degeneracy point appears at point K in the dispersion relationships along the first Brillouin zone shown in Fig. 2(c). When the lantern rings on pillars A and B are made of different materials (bronze alloy is used for lantern rings on pillars A; carbon steel is used for lantern rings on pillars B), the symmetry of the structure changes from C_{6v} to C_{3v}. The dispersion-relation curve is shown in Fig. 2(b), where the Dirac cone at point K is opened. K^+ and K^- are the corresponding extreme points (energy valleys). There is a huge energy difference between the two valleys; thus, energy cannot flow between them and a band gap forms. This is called the valley Hall effect, which is derived from the quantum valley Hall effect. In the dispersion curves, the color map indicates the polarization index [35], which is defined as

$$P_Z = \frac{\int_{V_u} |u_z|^2 dV}{\int_{V_u} (|u_x|^2 + |u_y|^2 + |u_z|^2) dV},$$

where V_u is the volume of the unit cell, and u_x, u_y, and u_z are the displacement components along the x, y, and z axes, respectively. P_Z would be close to one for out-of-plane modes and near zero for in-plane modes. It is shown that near the K point (valley mode), the fifth and sixth bands are

mainly for out-of-plane modes (red markers). Therefore, in this model, the out-of-plane vibration is considered.

III. VALLEY HALL EFFECT ANALOGY

For unit cells of types I (*A*-*B*) and II (*B*-*A*), shown in the left of Figs. 3(a) and 3(b), the corresponding valley modes of the phononic crystals are shown in the right of Figs. 3(a) and 3(b), respectively. The material settings of the lantern rings are the same as those outlined in Sec. II (bronze alloy is for *A*; carbon steel is for *B*). For the two cases, a Dirac cone in the top two bands is opened and a complete band gap is formed. The displacement fields located at the surface of the sample and energy-flow distributions of modes K_1–K_4 are calculated, as shown in Fig. 3(c). The energy, E_z, is defined and calculated via COMSOL as $E_z = (1/2)N_z\varepsilon_z$, where N_z is the internal force in the z direction, and ε_z is the internal strain in the z direction. The cyclic directions of the energy flux are represented by arrows. The energy-flux vectors of modes K_1 and K_2 are distributed in opposite directions. Modes K_3 and K_4 also have opposite energy-flux directions. In other words, K_1 (K_3) and K_2 (K_4) represent antichirality valley pseudospin modes, which are considered to be analogs of the electronic spin state. The existence of chiral or antichiral elastic energy-flux rotation is an important characteristic of valley modes, and the chiral or antichiral valley pseudospin modes of the elastic wave originate from the fact that valley modes carry an intrinsic orbital angular momentum. That is, the energy-flux rotation (pseudospin) represents the effective orbital angular momentum in the lattice. The spin-angular-momentum-density vector indicates the rotation of the displacement vector at any point per period. In addition, for unit cells of types I and II, the energy-flux cyclic directions of the top valleys are opposite, and the bottom valleys also have opposite energy-flux directions; this results from the difference in the elastic wave valley Hall phases.

The valley Chern number and Berry curvature are two important indices to characterize the topological nature of the band [36]. To further verify the generation of the topological phase transition in terms of physics, the quantitative Berry curvature and topological valley Chern number are calculated by using the discrete method. Compared with the qualitative method using the $k{\cdot}p$ perturbation theory, the discrete numerical method can capture changes to the valley Chern number and Berry curvature more accurately [37,38].

The valley phase can be characterized by using the valley Chern number, C_v^n, of the band, namely, $C_v^n = (1/2\pi)\int \Omega_n(\mathbf{k})d^2\mathbf{k}$, where Ω_n represents the Berry curvature of the nth band; $\mathbf{k}$ is the wave vector. The expression of Berry curvature is $\Omega_n(\mathbf{k}) = \nabla\mathbf{k} \times \mathbf{A}_n(\mathbf{k})$, where $\mathbf{A}_n$ is the Berry connection, a local gauge potential for Berry curvature, which is defined as $\mathbf{A}_n = \langle \mathbf{U}(\mathbf{k})|i\nabla\mathbf{k}|\mathbf{U}(\mathbf{k})\rangle$. In this case, $\mathbf{U}(\mathbf{k})$ denotes the displacement field in the z direction of the eigenmode calculated by the finite-element method using COMSOL. We consider a clockwise path around a certain point, $\mathbf{P}(k_x, k_y)$, consisting of $P_1(k_x - (\delta k_x/2), k_y - (\delta k_y/2))$, $P_2(k_x - (\delta k_x/2), k_y + (\delta k_y/2))$, $P_3(k_x + (\delta k_x/2), k_y + (\delta k_y/2))$, and $P_4(k_x + (\delta k_x/2), k_y - (\delta k_y/2))$. According to the Stokes theorem, we obtain $\int \Omega d^2\mathbf{k} = -\int B d\mathbf{k}$, where B is the Berry potential of a state defined by $\langle i\mathbf{U}(\mathbf{k})|\nabla\mathbf{k}|\mathbf{U}(\mathbf{k})\rangle$. For each patch $\delta k_x \times \delta k_y$, the Berry curvature and valley Chern number are calculated as

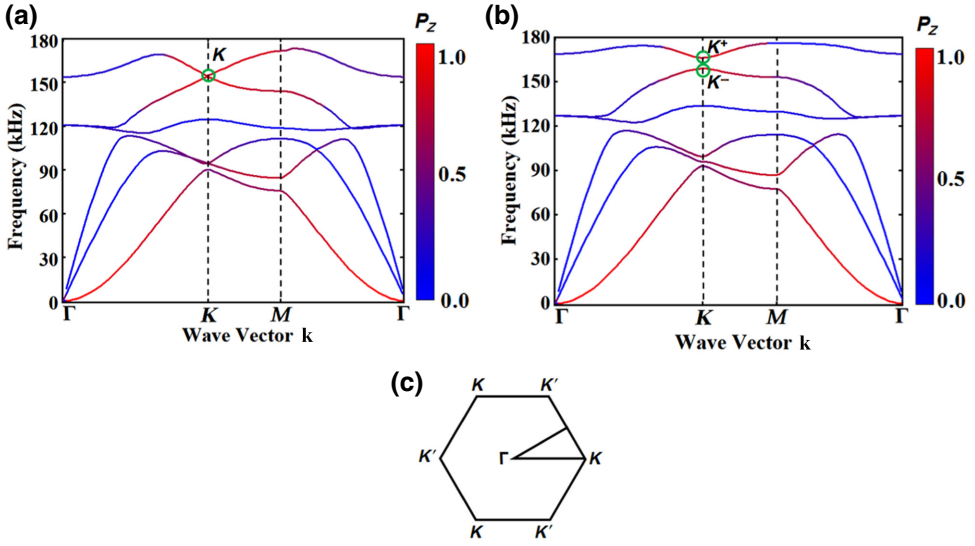

FIG. 2. Dispersion curves of unit cells. Color map indicates the polarization index, P_z. (a) Bronze alloy is used for lantern rings on pillars *A* and *B*. (b) Bronze alloy is used for lantern rings on pillars *A*, and carbon steel is used for lantern rings on pillars *B*. (c) First Brillouin zone.

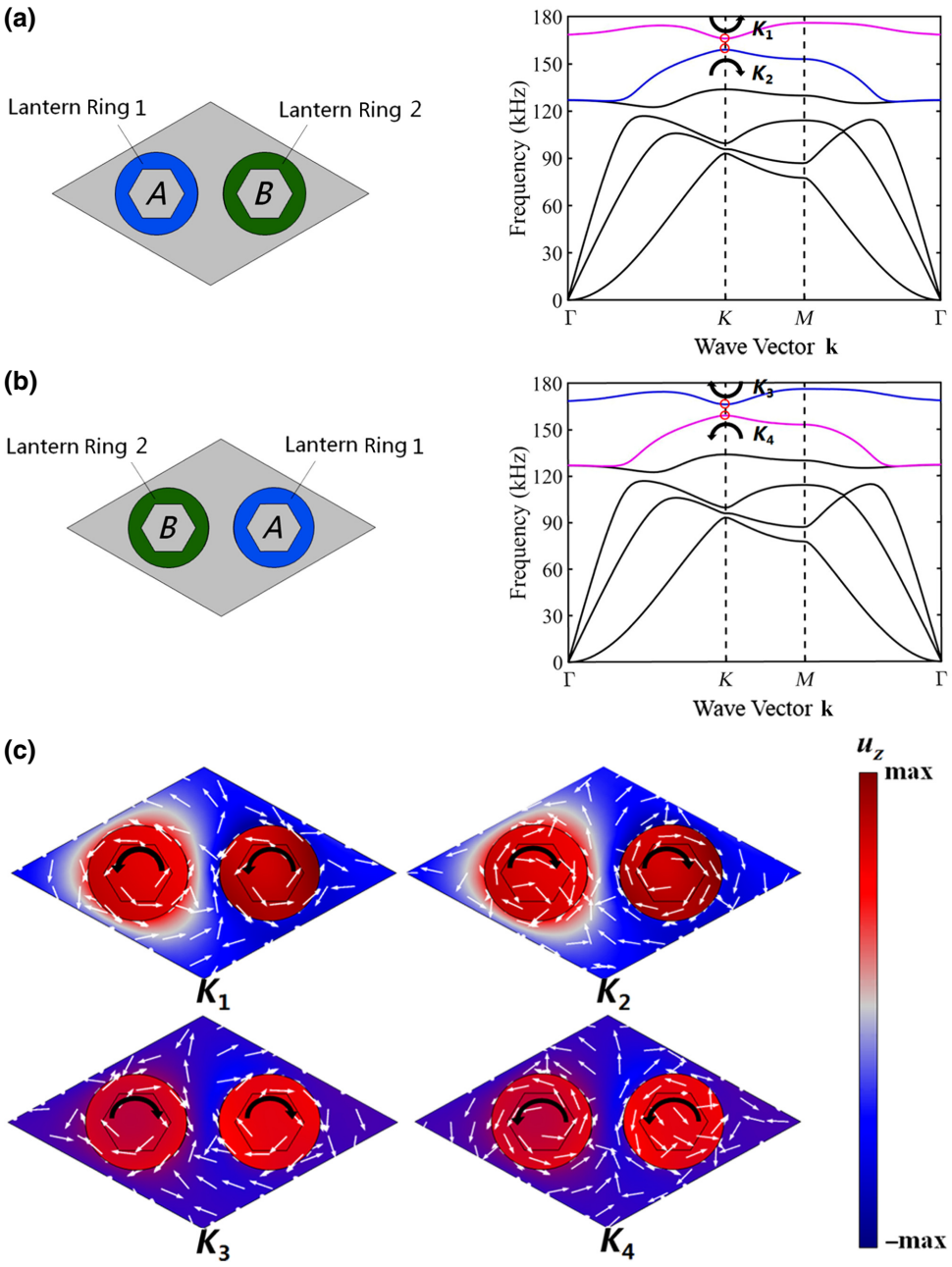

FIG. 3. Valley modes of phononic crystals with different unit-cell types. (a) Unit cell of type I (*A*-*B* type) and corresponding valley modes. (b) Unit cell of type II (*B*-*A* type) and corresponding valley modes. (c) Displacement fields and elastic energy fluxes of valley modes K_1–K_4.

$$\Omega_n(P) = \frac{\mathrm{Im}\left[\langle \mathbf{U}(P_1)|\mathbf{U}(P_2)\rangle + \langle \mathbf{U}(P_2)|\mathbf{U}(P_3)\rangle + \langle \mathbf{U}(P_3)|\mathbf{U}(P_4)\rangle + \langle \mathbf{U}(P_4)|\mathbf{U}(P_1)\rangle\right]}{\delta k_x \delta k_y}, \tag{1}$$

$$C_v^n = \frac{1}{2\pi} \sum_{\text{valley}} \Omega_n(\mathbf{P}). \tag{2}$$

The Berry-curvature distributions of the sixth and fifth bands of the unit cell of type I are shown in Figs. 4(a) and 4(b), respectively, and those of the unit cell of type II are shown in Figs. 4(c) and 4(d), respectively. It is shown that Berry curvatures are localized at the K and K' points and carry different signs. When the unit cell of type I is transformed into the unit cell of type II, there is a clear sign flip of the Berry curvature, suggesting that the topological phase transition happens during this process.

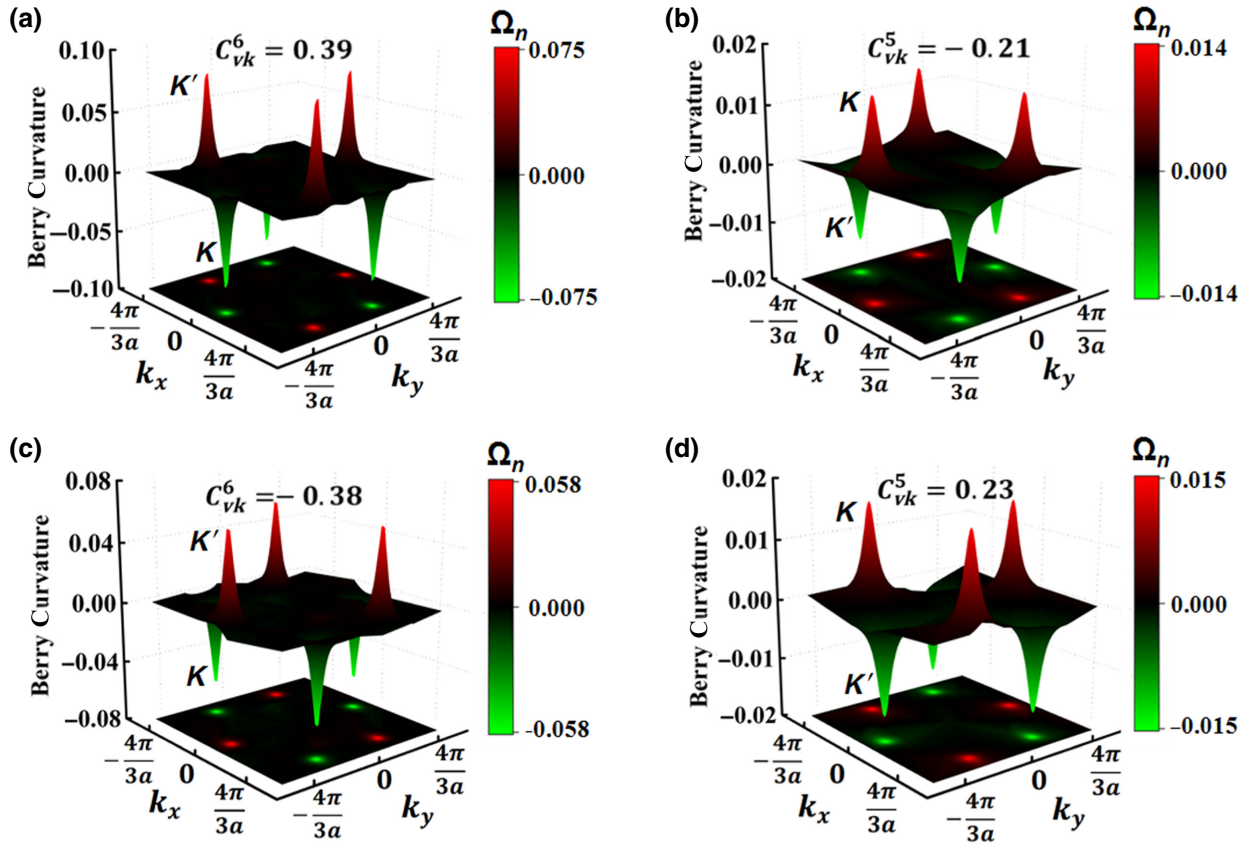

FIG. 4. Berry-curvature distributions of the unit cells: (a) sixth band of the unit cell of type I, (b) fifth band of the unit cell of type I, (c) sixth band of the unit cell of type II, (d) fifth band of the unit cell of type II.

Through the numerical integration of Eq. (2) over a local square region around the Dirac points, the valley Chern numbers, C_v^n, are obtained, as shown in Figs. 4(a)–4(d). For the unit cell of type I, the top and bottom modes at the K valley carry Chern numbers of $C^6_{vk} = 0.39$ and $C^5_{vk} = -0.21$, respectively. Those of the unit cell of type II are $C^6_{vk} = -0.38$ and $C^5_{vk} = 0.23$, respectively. For the two types of unit cells, the signs of valley Chern numbers are inverse; this distinguishes the topological phase of the structure. Therefore, if phononic crystals with the two types of unit cells are combined together, there is a phase transition at the interface, which is an essential condition for forming topological edge states. Numerical integrations of Eq. (2) over a small square region around the Dirac points give Chern numbers with absolute values less than 0.5. Deviations are caused by the strong space-inversion symmetry breaking [39,40]. In fact, the weaker the space-inversion symmetry breaking, the more the Berry curvature is localized at the Dirac point, and the valley Chern number approaches ± 0.5.

The influences of variations in the Young's modulus and density of the lantern-ring materials on the valley band gap are further analyzed. Here, only out-of-plane vibrations are taken into account; thus, the Poisson ratio of the lantern-ring materials is not considered. First, the Young's modulus of the right lantern ring in the unit cell is fixed as 180 GPa and that of the left lantern ring is increased from 80 to 260 GPa or decreased inversely gradually. The calculated frequency bands, according to the difference in the Young's modulus (ΔE) between materials of the two types of lantern rings, are shown in Figs. 5(a)–5(c). The densities of the left lantern rings in Figs. 5(a)–5(c) are fixed as 7900 kg/m^3; the densities of the right ones are 7900, 3000, and 1000 kg/m^3 in Figs. 5(a)–5(c), respectively. Under the condition of $\Delta\rho = 0$, it can be seen that, in Fig. 5(a), when $\Delta E \neq 0$, the band gap opens up. The size of the band gap increases with the increase of the absolute value of ΔE. The maximum value of the band gap is 6.73 kHz. For $\Delta\rho = 4900$ in Fig. 5(b) and 6900 kg/m^3 in Fig. 5(c), the maximum band-gap values are 14.28 and 17.61 kHz, respectively. The density differences in two kinds of lantern-ring materials, besides Young's modulus differences, result in larger band gaps. The midgap frequency is defined as the intermediate value of the top-band frequency, f_{top}, and the bottom-band frequency, f_{bottom}, of the band gap, namely, $f_{\text{midgap}} = f_{\text{bottom}} + (1/2)(f_{\text{top}} - f_{\text{bottom}})$. The midgap frequency of the bands increases obviously with the increase in ΔE. This is

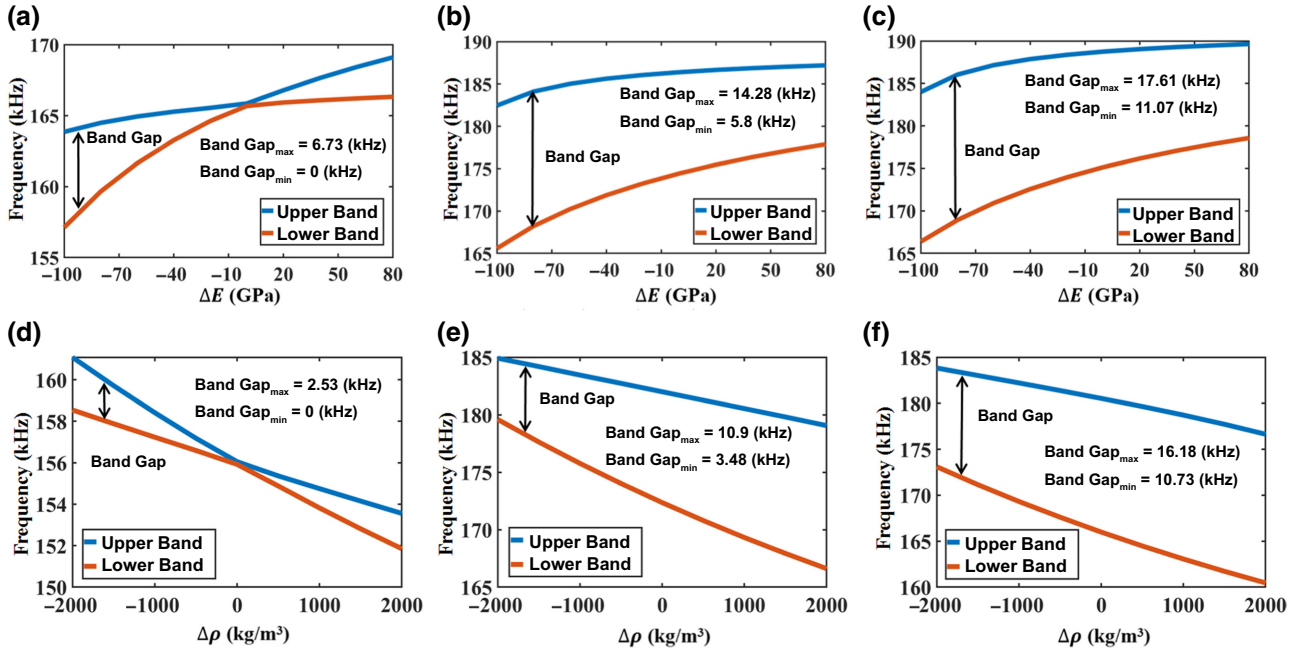

FIG. 5. Variations in the topological band gap by changing lantern-ring materials. Influence of the difference in Young's modulus (ΔE) on the frequency band: $\Delta\rho = 0$, 4900, and 6900 kg/m^3 in (a)–(c) respectively. Influence of the density difference ($\Delta\rho$) on the frequency band: $\Delta E = 0$, 162, and 216 kg/m^3 in (d)–(f), respectively.

because the propagation velocity of elastic waves is influenced by variations in the Young's modulus of lantern-ring materials.

To analyze the influence of the density difference, the density of the right lantern-ring material is fixed as 7900 kg/m^3 and that of the left lantern ring is increased from 5900 to 9900 kg/m^3 or decreased inversely gradually. The calculated frequency bands, according to the difference in density ($\Delta\rho$) between materials of the two types of lantern rings, are shown in Figs. 5(d)–5(f). The Young's moduli of the left lantern rings in Figs. 5(d)–5(f) are fixed as 270 GPa; those of the right lantern rings are 270, 108, and 54 GPa in Figs. 5(d)–5(f), respectively. It is shown that the maximum values of the band gaps are 2.53, 10.9, and 16.18 kHz for $\Delta E = 0$, 162, and 216 GPa, respectively. In addition, the midgap frequency of the bands decreases obviously with the increase of $\Delta\rho$. The above results indicate that differences in the Young's modulus and density of lantern-ring materials can both lead to the opening of Dirac cones. Some typical materials are selected to calculate the topological band-gap values, which are shown in Table I. It can be seen that the required band gap can be obtained by selecting suitable lantern-ring materials.

IV. VALLEY-DEPENDENT EDGE STATES

To verify the existence of topological valley edge states, two types of supercells are constructed by connecting lattices based on unit-cell types I and II, as shown in Figs. 6(a) and 6(b), respectively. For supercell I, lattices based on

TABLE I. Calculated topological band-gap values based on typical materials.

Combination No.	Material A (E, GPa; ρ, kg/m^3)	Material B (E, GPa; ρ, kg/m^3)	Band gap (kHz)
1	Steel (185, 7850)	Lithium (4.9, 534)	18.04
2	Lead (16, 11 730)	Lithium (4.9, 534)	16.13
3	Magnesium (45, 1700)	Lead (16, 11 730)	10.57
4	Bronze alloy (80, 8640)	Carbon fiber T700 (2 101 740)	16.97
5	Silicon carbide (400, 3073)	Brass H62 (105,8400)	17.36
6	Carbon fiber T700 (210, 1740)	Lithium (4.9, 534)	32.53
7	Lead (16, 11 730)	Gray cast iron (1 207 000)	12.71
8	Zirconium oxide (220, 6000)	Lithium (4.9, 534)	22.33
9	Carbon fiber T700 (210, 1740)	Magnesium (45, 1700)	17.18
10	Silicon carbide (400, 3073)	Lithium (4.9, 534)	32.23

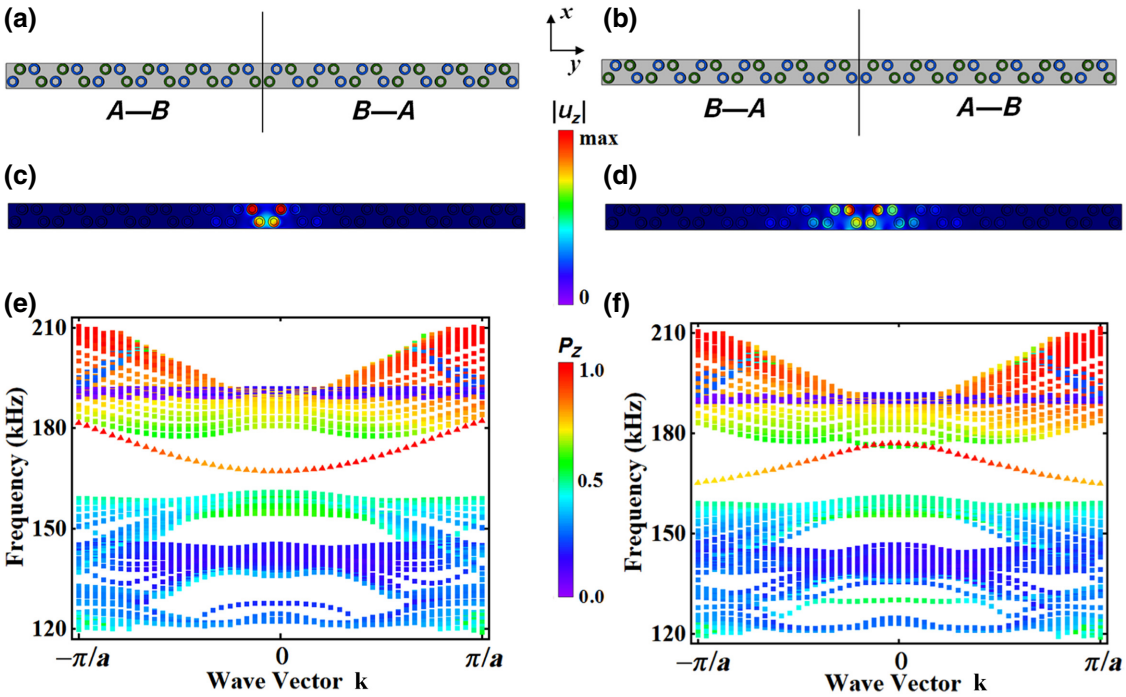

FIG. 6. (a) Supercell I; a is the lattice constant. (b) Supercell II. (c) Displacement-amplitude distribution of supercell I. (d) Displacement-amplitude distribution of supercell II. (e) Band structure of supercell I; **k** is the wave vector in the x direction. (f) Band structure of supercell II. In (e),(f), triangles denote valley edge states; squares correspond to bulk states.

unit-cell type I are on the left, and those based on unit-cell type II are on the right. For supercell II, the arrangement is reversed. Periodic boundary conditions are enforced along the x direction to simulate a continuous plate. The top and bottom boundaries along the y direction are assigned as free boundary conditions. The dispersion relationships of the two types of supercells are calculated, as shown in Figs. 6(e) and 6(f), respectively. In the dispersion curves, the color map indicates the polarization index, P_z. The valley Hall edge states can be observed in the frequency range from 167 to 178 kHz for supercells I and II. The edge states are indicated by triangles, and the squares correspond to bulk states. The displacement-amplitude distributions of these two types of supercells for an edge-state frequency of 172 kHz are calculated, as shown in Figs. 6(c) and 6(d), respectively. The results indicate that the domain walls can effectively support edge states. For the edge state in supercell I, the vibration-displacement strength and the energy-concentration degree are higher than those for supercell II. Thus, the domain wall in supercell I is chosen to illustrate the behavior of backscattering suppression and defect immunity of the edge state in the following discussion.

To examine the elastic-wave-transport characteristics in the phononic crystal structure, straight and Z-shaped waveguides are constructed. The elastic-wave-transmission effects are examined by simulation and experimental methods. The transmission input is located at the entrance of the waveguide path; the transmission output is located at the end of the waveguide path. The transmission is defined as $T = S_{\text{out}}/S_{\text{in}}$, where S_{out} is the displacement of the transmission output and S_{in} is the displacement of the transmission input. The sample, experiment sets, and principles of measurement are shown in Fig. 7. A laser Doppler vibrometer (LV-S01) is used to test the displacement fields of the sample, which is shifted using a precision translation platform (PSA500-11-X). A Rigol DG1022U arbitrary function generator is used to generate sine excitation waveforms. The excitation signal is further amplified to $200V_{\text{pp}}$ by a Trek PZD700A wideband power amplifier and applied to a piezoelectric transducer at the entrance of the waveguide, which is used to excite the out-of-plane vibrations. Additionally, the borders of the sample are coated with absorbing materials (photoresist and silica gel) to avoid wave scattering from the boundary. During scanning, the laser beam from the vibrometer is perpendicular to the sample and only the vertical displacement component (z component) is captured.

For the straight waveguide, a defect is set in the middle of the waveguide path, namely, two lantern rings made of carbon steel are taken away, as shown in the local image in Fig. 8(a). The Z-shaped waveguide [Fig. 8(b)] is used to examine the ability of the phononic crystal structure to suppress scattering when corners emerge in the waveguide path. Frequencies of 150–180 kHz (step width is 1 Hz) are chosen for the excitation signals. Sweep-frequency

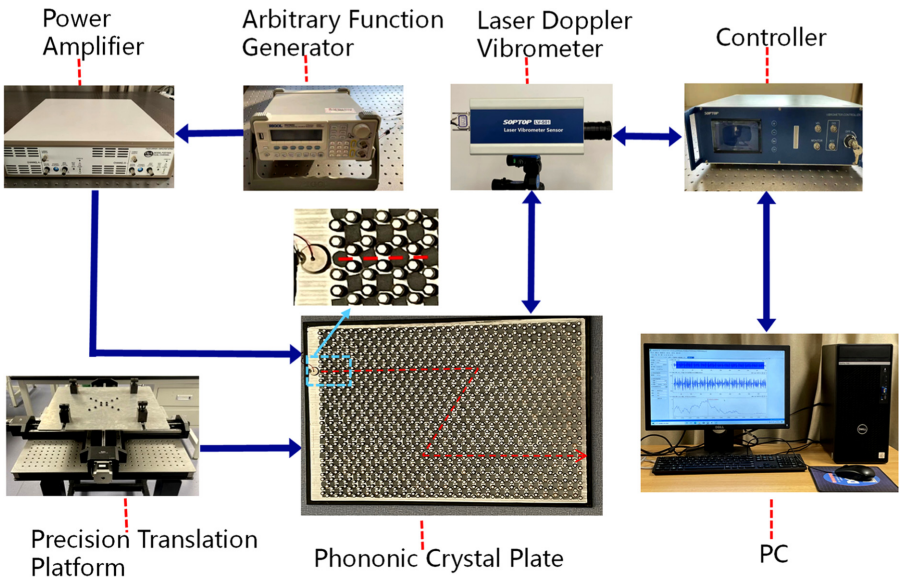

FIG. 7. Photograph of the fabricated sample and a flow chart of the vibration test.

measurements on the displacement field of the sample are conducted for the above frequency range. The measurements for each frequency at each location are conducted 5 times; displacement values obtained 5 times are averaged.

The simulations are conducted via COMSOL Multiphysics. The solid mechanics module is used to model the phononic crystal structure; a frequency-domain analysis is carried out to simulate wave propagation. A wave source (same as that in the experiment) is set at the entrance of the waveguide. During finite-element-method simulations, an absorbing boundary condition is applied to four outer edges of the phononic crystal plate to prevent wave reflections from the boundaries. The frequency-scanning range for the simulation is the same as that for the experiment.

Figures 8(c) and 8(d) show the simulation and experimental results, respectively, of the displacement-field distribution of the straight waveguide shown in Fig. 8(a). The frequency of the edge state is 172 kHz. The elastic wave energy is well localized along the interface between the two domain walls. Near the defect, the scatterings are slightly stronger. After passing through the defect, the elastic wave can still propagate along the waveguide. Figures 8(e) and 8(f) show the results of the Z-shaped waveguide for the edge state at 172 kHz. Even if there are bending corners in the waveguide's path, backscattering

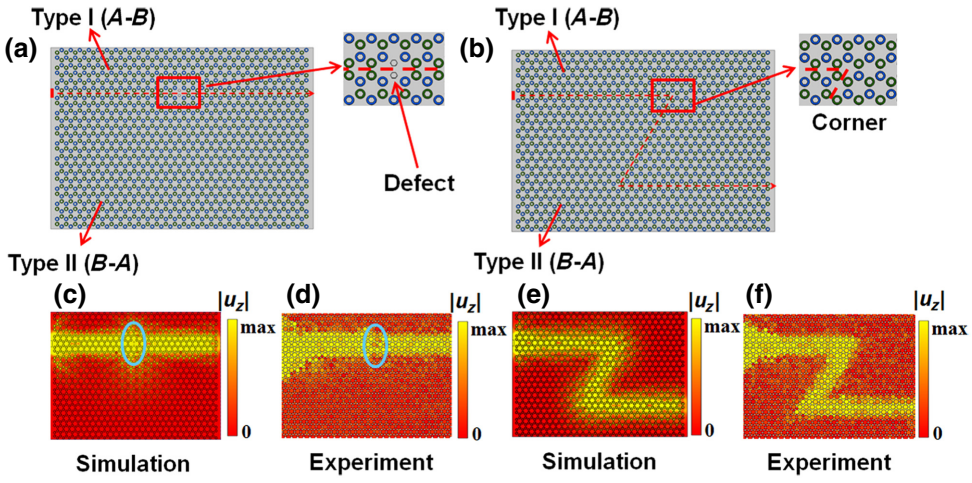

FIG. 8. Topologically protected waveguides based on the edge state at 172 kHz for phononic crystals with bronze-alloy and carbon-steel lantern rings. (a) Straight path with a defect. (b) Z-shaped path. (c),(d) Simulation and experimental results, respectively, for topological transport of a straight waveguide with a defect. (e),(f) Simulation and experimental results, respectively, for topological transport of a Z-shaped waveguide.

is minimal and the energy loss in the propagation process is very small. The simulation and experimental results indicate that stable edge-state transmissions of the elastic wave can be realized in this phononic crystal structure. In Figs. 8(c)–8(f), the path width in the experimental results are a little larger than those in the simulation results. This can be attributed to manufacturing deviations of the sample, which influence the degree of energy concentration.

To be more quantitative, the transmission-frequency curves of the edge state that propagates along the straight and Z-shaped waveguides shown in Fig. 8 are measured, as shown in Fig. 9. The simulation results are also presented. Slight differences exist between the transmission curves obtained by numerical calculations and experimental measurements; these are caused by machining tolerances of the sample. It is shown that, for the frequency range from 166.1 to 176.3 kHz, the transmission of the edge states in the straight waveguide is obviously higher than that for frequencies out of this range. For the Z-shaped waveguide, the frequency range with higher transmissions is 166.4–176.1 kHz. The two frequency ranges agree approximately with that of the edge states shown in Fig. 6(e) (167–178 kHz). It is indicated that different valley Hall phases can be realized by changing the lantern-ring materials of the phononic crystals, based on which, the edge states emerge at the interface between the two domain regions with a phase transition.

To present the tunability of the operating frequency, lantern rings made of another kind of material are introduced. Titanium alloy is selected as the third material to replace lantern-ring material *B* (carbon steel), and lantern-ring material *A* remains unchanged (bronze alloy). A straight path with a defect and a Z-shaped path, the same as those in Fig. 8, are set. Frequencies of 170–200 kHz (step width is 1 Hz) are chosen for the excitation signals. Sweep-frequency measurements on the displacement field of the sample are conducted for this frequency range. Figure 10 shows topologically protected waveguides based on the edge state at 189 kHz: (a) and (b) are simulation and experimental results, respectively, for a straight path with a defect; (c) and (d) are simulation and experimental results, respectively, for a Z-shaped path. In Figs. 10(a)–10(d), it is shown that, at the operating frequency of 189 kHz, topologically protected stable waveguides can be obtained.

When lantern-ring material *B* (carbon steel) is replaced by titanium alloy, the topological operating-frequency range changes to 182–192 kHz, which is shown in the transmission spectra [Figs. 10(e) and 10(f)]. When lantern-ring material *B* is carbon steel, the topological operating-frequency range is about 166–176 kHz, as shown in Fig. 9. It can be seen that the operating frequency can indeed be altered conveniently by changing the lantern-ring material.

Additionally, more materials are used to replace lantern material *B*; the calculated operating-frequency ranges are shown in Table II. It can be seen that a sufficiently large tunability of the operating frequency can be obtained by changing the lantern-ring materials.

To capture the topological phase-transition process when changing continuously the material parameters, evolutions of the Berry curvature and valley Chern number when varying continuously the Young's moduli and densities of the lantern rings in the unit cell of type I are calculated by using Eqs. (1) and (2), and the physical mechanism for the generation of topological edge states utilizing the change of lantern-ring material parameters is clarified. First, the densities of the two sets of lantern rings are set to be the same (7900 kg/m^3), and the difference in the Young's moduli is changed (the Young's modulus of the right lantern ring in the unit cell is fixed as 180 GPa and that of the left lantern ring is increased from 60 to 300 GPa or decreased inversely gradually). Evolutions of the valley Berry curvature, Chern number, and Dirac band gap are shown in Fig. 11(a).

In Fig. 11(a), corresponding to the difference in the Young's modulus (ΔE), the evolution of the Dirac band gap is shown as a solid blue line. Near the solid blue line, the corresponding Berry-curvature distributions and valley Chern numbers of some points are presented. It

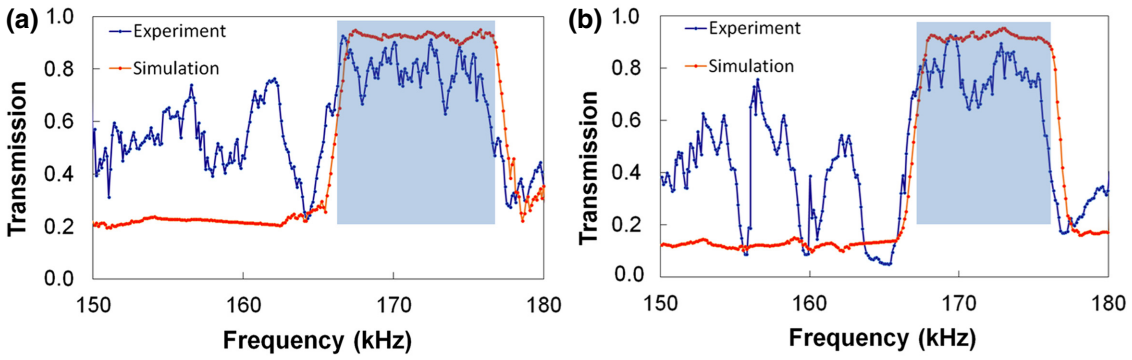

FIG. 9. Transmission spectra for phononic crystals with bronze-alloy and carbon-steel lantern rings: (a) straight waveguide and (b) Z-shaped waveguide.

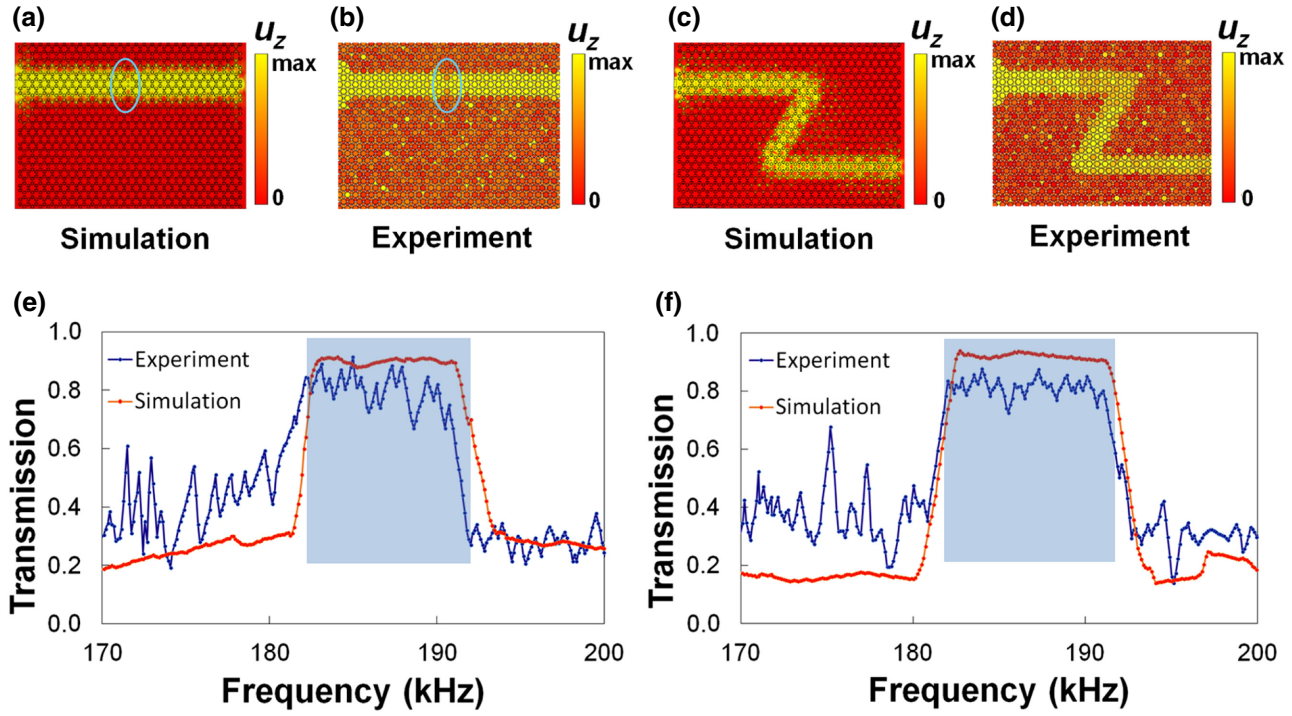

FIG. 10. Topological transport effects of phononic crystals with bronze-alloy and titanium-alloy lantern rings. (a),(b) Simulation and experiment results, respectively, for topological transport at 189 kHz of a straight waveguide with a defect. (c),(d) Simulation and experiment results, respectively, for topological transport at 189 kHz of a Z-shaped waveguide. (e),(f) Transmission spectra for a straight waveguide with a defect and Z-shaped waveguide, respectively.

can be seen that, with an increase of ΔE from -120 to 120 GPa, the band gap of the two eigenbands closes and then reopens. Before and after $\Delta E = 0$, sign reversal of the Berry curvatures occurs. The sign of the Berry curvature indicates the valley topological phase. Thus, this reveals that the topological phase transition happens as the sign of ΔE changes from positive to negative (or inversely). Therefore, when two types of phononic crystals with different signs of ΔE form an interface, valley topologically protected interface modes can be obtained, which results from the topological phase transition originating from the equivalent space-inversion symmetry breaking.

In Fig. 11(a), when increasing the absolute value of ΔE, the magnitude of the Berry curvature becomes smaller and the distribution becomes dispersed (a blunter shape of the Berry curvature is obtained), which results in a decrease in the valley Chern number. This verifies that the degree of equivalent space-symmetry breaking becomes stronger with an increase in the absolute value of ΔE. When $\Delta E = 0$, space-symmetry breaking is absent, so the band gap of the two eigenbands closes completely, which results in the disappearance of the topological edge states. Then, the Young's moduli of the two sets of rings are set to be the same (54 GPa), and the density difference is changed (the density of the right lantern-ring material is fixed as 7900 kg/m^3 and that of the left lantern ring is increased from 3900 to 11 900 kg/m^3 or decreased inversely gradually). Evolutions of the valley Berry curvature, Chern number, and band gap are shown in Fig. 11(b); similar conclusions to the case of the changing Young's modulus are obtained.

It can be seen that the variation in the material parameters does change the degree of symmetry breaking of equivalent space inversion. Breaking the symmetry of

TABLE II. Tunable topological-mode operating frequencies by changing the lantern-ring material on pillar *B*.

Combination No.	Material *A* (*E*, GPa; ρ, kg/m$\supset$3)	Material *B* (*E*, GPa; ρ, kg/m$\supset$3)	Frequency range (kHz)
1	Bronze alloy (80, 8640)	Carbon steel (185, 7900)	166–176
2	Bronze alloy (80, 8640)	Titanium alloy (110, 4500)	181–191
3	Bronze alloy (80, 8640)	Aluminum (70, 2700)	192–205
4	Bronze alloy (80, 8640)	Lithium (4.9, 534)	136–157

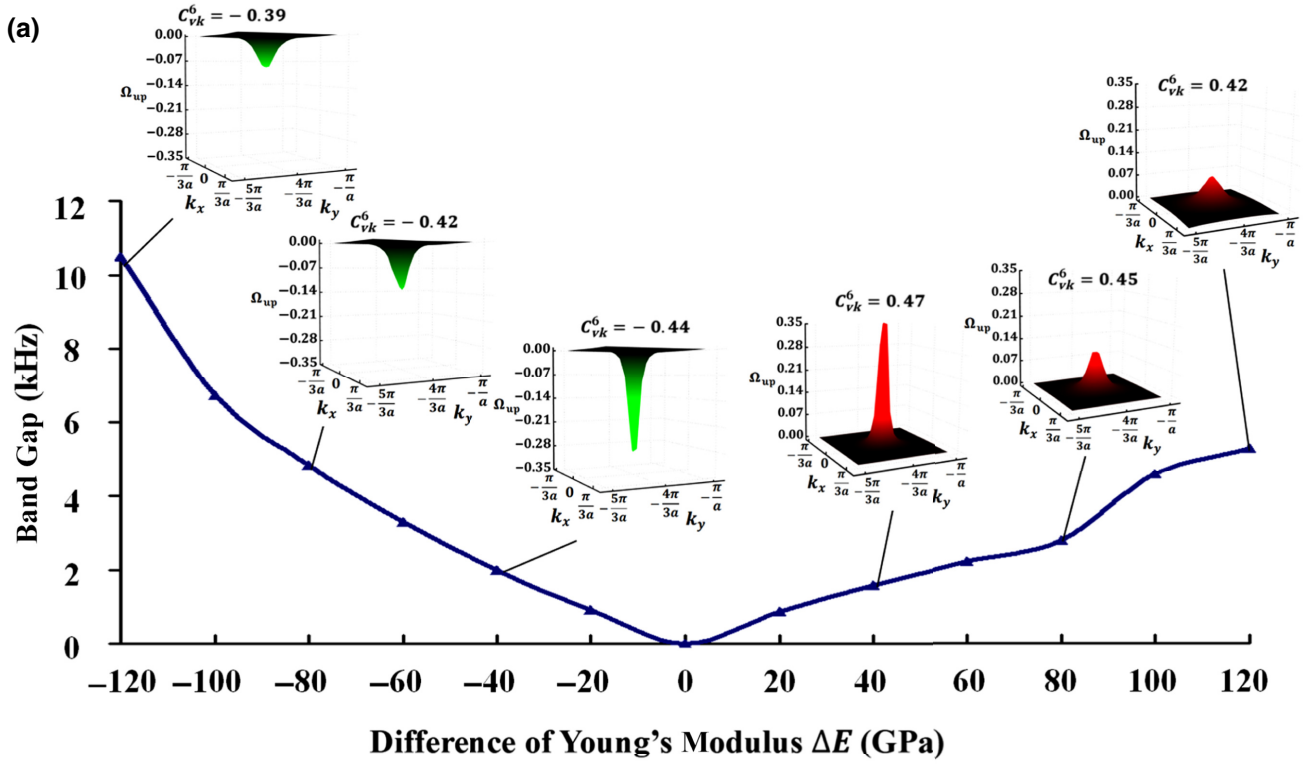

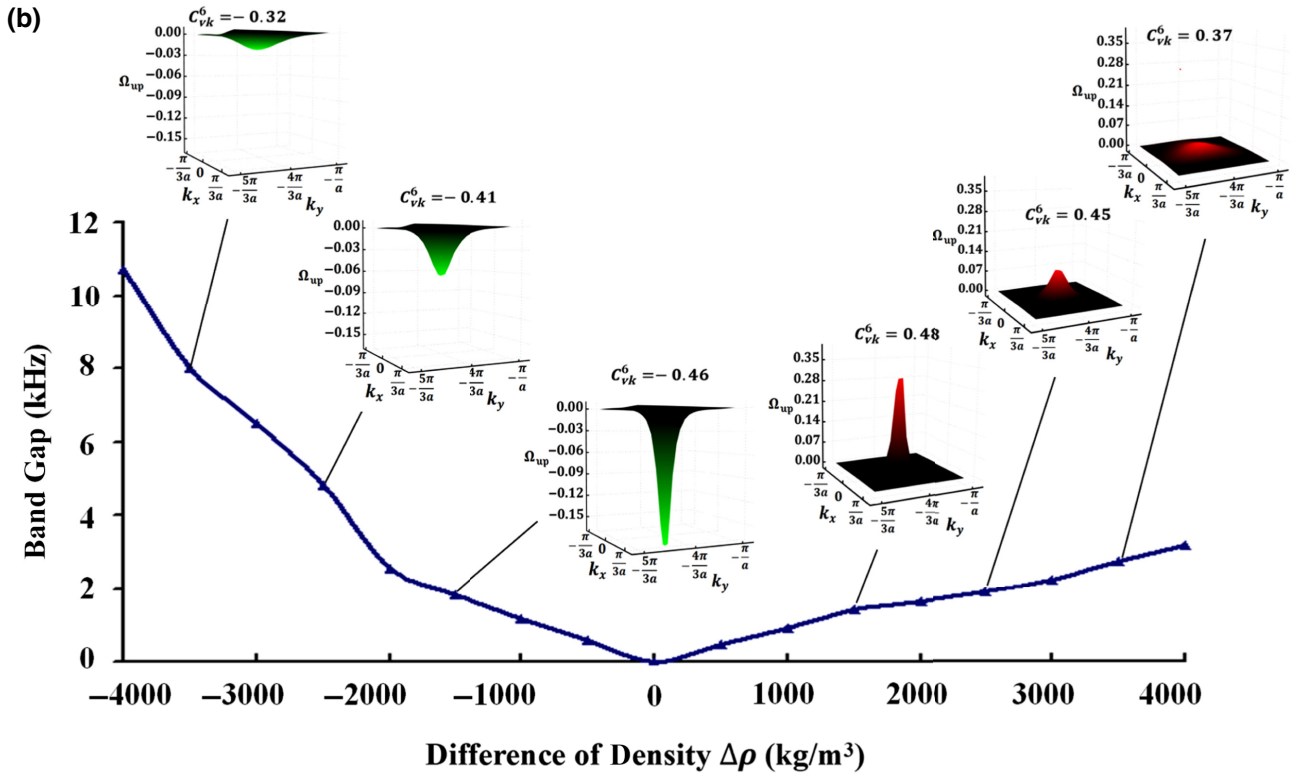

FIG. 11. Evolutions of the Berry curvature, valley Chern number, and band gap when varying continuously the material parameters of lantern rings: (a) Young's modulus, (b) density.

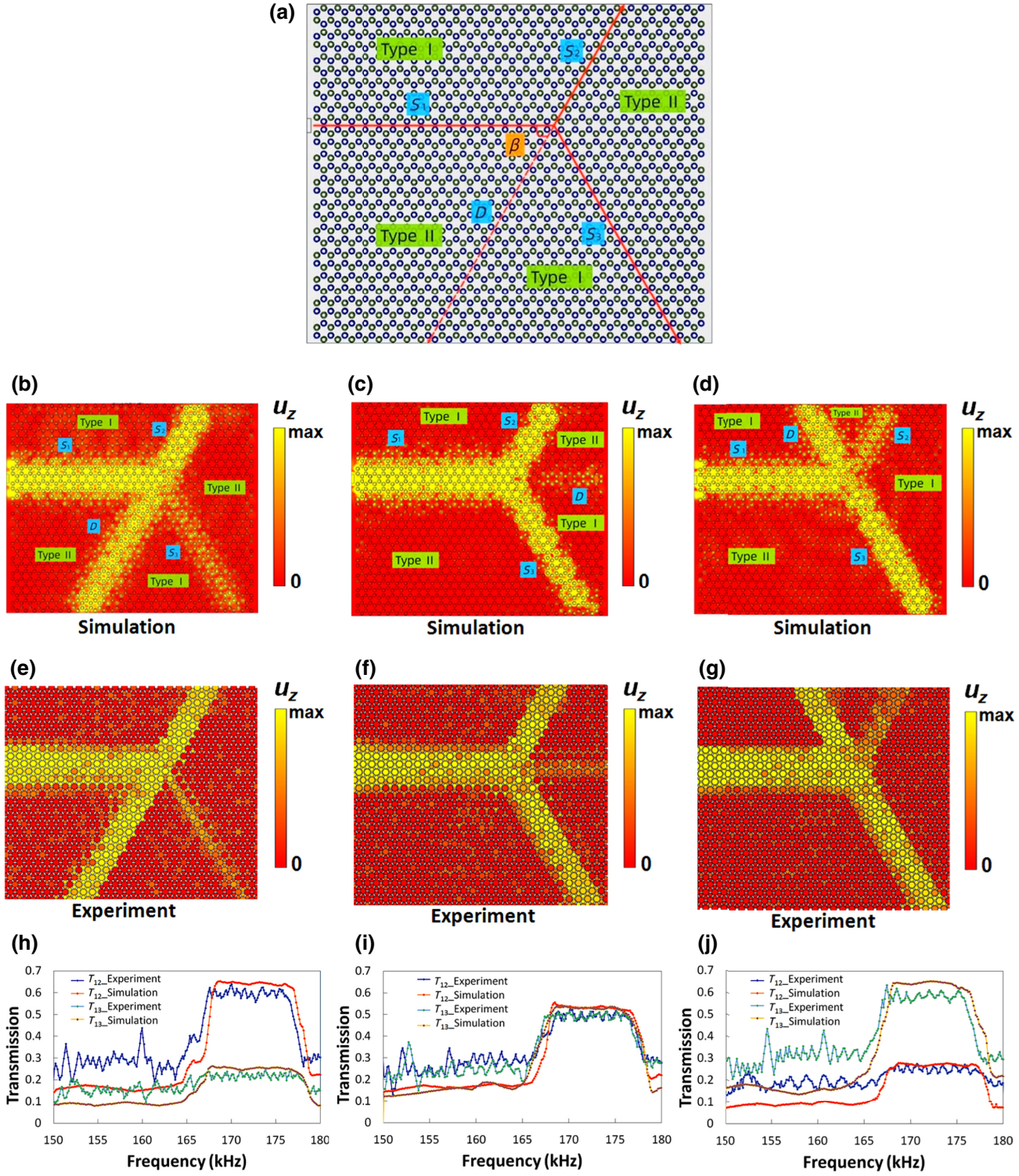

FIG. 12. Reconfigurable cross-waveguide splitter. (a) Schematic diagram of the path design. (b)–(d) Simulation results of transmission effects of three types of cross-waveguide splitters for $\beta = 60°$, 180°, and $-60°$, respectively. (e)–(g) Experimental results for the transmission effects of three types of cross-waveguide splitters for $\beta = 60°$, 180°, and $-60°$, respectively. (h)–(j) Transmission spectra of three types of cross-waveguide splitters for $\beta = 60°$, 180°, and $-60°$, respectively. T_{ij} represents the transmission spectrum from port S_i to port S_j ($i = 1$ and $j = 2, 3$).

equivalent space to a greater extent can be realized conveniently by the method presented here, namely, by selecting lantern-ring materials with a larger parameter difference.

V. RECONFIGURABLE CROSS-WAVEGUIDE SPLITTER

A reconfigurable cross-waveguide splitter is designed, as shown in Fig. 12(a). This splitter consists of four sections consisting of phononic crystals with unit-cell types I or II. Four topological edge states are formed. Three fixed channels are labeled by S_1, S_2, and S_3, and one channel is changeable, which is labeled by D. S_1 is the input channel, the others are output channels. The angle between the changeable channel D and fixed channel S_1 is denoted by β.

To further characterize the cross-waveguide splitter, a full-field numerical out-of-plane elastic wave transport simulation and experimental validation are performed, and the material and dimension parameters used are the same as those in Sec. II. Details of settings in the simulations are the same as those in Sec. IV. Specifically, three types of splitters are obtained through changing the position of channel D, namely, the angle β is selected to be 60°, 180°, and −60°. For the simulation and experiment, the wave source at the entrance of the waveguide is an out-of-plane sinusoidal harmonic vibration with a frequency of 172 kHz. The simulation results for transmission of the three waveguide splitters are shown in Figs. 12(b)–12(d); the corresponding experiment results are shown in Figs. 12(e)–12(g), respectively.

In fact, channel D plays a role in the transmission ratio between the edge modes of channels S_2 and S_3. For $\beta = 180°$, the simulated transmission ratio between channels S_3 and S_2 shown in Fig. 12(c) is 0.96, which approximately agrees with the experimental value of 0.92. That is, the vibration strengths of channels S_2 and S_3 are approximately equal, which can also be seen in the transmission spectra in Fig. 12(i). In the transmission spectra, T_{ij} represents the transmission spectrum from port S_i to port S_j ($i = 1$ and $j = 2, 3$). For $\beta = 60°$ shown in Fig. 12(b), the simulated transmission ratio between channels S_3 and S_2 becomes 0.33 (the experimental value is 0.30), which is less than that with a β value of 180°, and more energy tends to transfer into channel S_2. This is also shown in the transmission spectra in Fig. 12(h). Under this condition, phononic crystals of type II and type I are, respectively, located on the left and right sides of channel S_3, namely, the phononic crystal types located on both sides of S_3 are inverse compared with the other three channels. Thus, channel S_3 corresponds to the interface-state type II described in Figs. 6(b) and 6(d), the scattering of which is stronger and the vibration in the channel is weaker compared with interface-state type I. Therefore, this leads to weaker wave transmission in channel S_3. For $\beta = -60°$, the simulated transmission ratio between channel S_3 and S_2 is 2.7 (the experimental value is 3.1), which is larger than those with β values of 180° and 60°, and more energy tends to transfer into channel S_3, which can also be seen in the transmission spectra in Fig. 12(j). This path distribution makes channel S_2 belong to interface-state type II, which leads to a weaker transmission of channel S_2. Consequently, through changing the location of one output channel, the transmission ratio between the other two output edge modes in the cross-waveguide splitter can be controlled effectively. The wave splitter proposed in this work has the feature of reconfiguration. In other words, through the rearrangement of lantern rings, different transmission ratios among output branches of the wave splitter can be obtained conveniently. In addition, the operating frequency of the wave splitter can be tuned easily by changing the lantern-ring materials.

For the reconfigurable splitting of topologically protected elastic edge states, applications in elastic wave devices, such as splitters and signal processing in a monolithic elastic network [41,42], could be realized in the future.

VI. CONCLUSIONS

Here, the topological valley transport edge states of elastic waves are realized based on material differences. It is shown that differences in the Young's modulus and density of lantern-ring materials can cause the destruction of the effective spatial inversion symmetry, which gives rise to the valley Hall phase transition, and thus, leads to the formation of topological edge states. The evolution processes of the Berry curvature and topological valley Chern number, when varying continuously the material parameters of lantern rings, are revealed; the topological phase transition caused by changing the lantern-ring material is captured; and the physical mechanism for the generation of topological edge states, utilizing changes of lantern-ring material parameters, is clarified. The results show that the topological valley transport of elastic waves has no obvious backscattering at bending corners of the waveguide and has a certain immunity to defects. By rearranging the lantern rings, any waveguide path with topological valley transport can be realized conveniently. As an application case, a reconfigurable cross-waveguide splitter of topological elastic edge states is realized. For valley topological edge states, the traditional method to break the spatial inversion symmetry is to change the structural parameters of the scatterers in the phononic crystal. However, in many application cases, topological band-gap sizes obtained by this method are limited, which restricts the frequency range of the topological edge states obviously. Additionally, after sample fabrication is finished, it is difficult to change the transport path and operating-frequency range of elastic waves. Here, the above problems are solved by

realizing valley topological transport based on changes to the lantern-ring materials. The transport path can be easily altered, and the operating frequency can be tuned conveniently by changing the lantern-ring materials, which is very important for topological transport of elastic waves. The realization of topological edge states based on material differences provides an effective method for achieving the topological transport of elastic waves, breaking the limitations of those based only on structural parameter changes, and has a good application prospect in the field of elastic wave manipulation and communication.

ACKNOWLEDGMENTS

This work is supported by the National Natural Science Foundation of China (Grants No. 12172183, No. 11772163, and No. 12072167); the Natural Science Foundation of Zhejiang Province (Grant No. LY21A020007); the One Health Interdisciplinary Research Project; Ningbo University; and the Natural Science Foundation of Ningbo City, China (Grant No. 2022J090). Professor Iren Kuznetsova and Dr. Ilya Nedospasov thank the Russian Ministry of Science and Higher Education (Grant No. FFWZ-2022-0002) for partial financial support.

[1] Y. F. Wang, Y. Z. Wang, B. Wu, W. Q. Chen, and Y. S. Wang, Tunable and active phononic crystals and metamaterials, Appl. Mech. Rev. **72**, 040801 (2020).

[2] Y. Y. Chen, X. P. Li, G. K. Hu, M. R. Haberman, and G. L. Huang, An active mechanical Willis meta-layer with asymmetric polarizabilities, Nat. Commun. **11**, 3681 (2020).

[3] P. Li, G. Wang, D. Luo, and X. S. Cao, Wave bandgap formation and its evolution in two-dimensional phononic crystals composed of rubber matrix with periodic steel quarter-cylinders, Int. J. Mod. Phys. B **32**, 1850037 (2018).

[4] L. Y. Yao, G. L. Huang, H. Chen, and M. V. Barnhart, A modified smoothed finite element method (M-SFEM) for analyzing the band gap in phononic crystals, Acta Mech. **230**, 2279 (2019).

[5] D. L. Yu, J. H. Wen, H. G. Zhao, Y. Z. Liu, and X. S. Wen, Vibration reduction by using the idea of phononic crystals in a pipe-conveying fluid, J. Sound Vib. **308**, 193 (2008).

[6] Y. F. Wang, Y. S. Wang, and L. T. Wang, Two-dimensional ternary locally resonant phononic crystals with a comblike coating, J. Phys. D: Appl. Phys. **47**, 015502 (2014).

[7] X. Zhang and Z. Liu, Negative refraction of acoustic waves in two-dimensional phononic crystals, Appl. Phys. Lett. **85**, 341 (2004).

[8] M. H. Lu, C. Zhang, L. Feng, J. Zhao, Y. F. Chen, Y. W. Mao, J. Zi, Y. Y. Zhu, S. N. Zhu, and N. B. Ming, Negative bi-refraction of acoustic waves in a sonic crystal, Nat. Mater. **6**, 744 (2007).

[9] W. X. Jiang, T. J. Cui, G. X. Yu, X. Q. Lin, Q. Cheng, and J. Y. Jin, Arbitrarily elliptical–cylindrical invisible cloaking, J. Phys. D: Appl. Phys. **41**, 085504 (2008).

[10] S. X. Yang, J. H. Page, Z. Y. Liu, M. L. Cowan, C. T. Chan, and P. Sheng, Focusing of Sound in a 3D Phononic Crystal, Phys. Rev. Lett. **93**, 024301 (2004).

[11] C. Y. Qiu, Z. Y. Liu, and J. Shi, Directional acoustic source based on the resonant cavity of two-dimensional phononic crystals, Appl. Phys. Lett. **86**, 224105 (2005).

[12] A. B. Khanikaev, S. H. Mousavi, W. K. Tse, M. Kargarian, A. H. MacDonald, and G. Shvets, Photonic topological insulators, Nat. Mater. **12**, 233 (2013).

[13] J. Mei, Y. Wu, C. T. Chan, and Z. Q. Zhang, First-principles study of Dirac and Dirac-like cones in phononic and photonic crystals, Phys. Rev. B **86**, 035141 (2012).

[14] Y. Li, Y. Wu, and J. Mei, Double Dirac cones in phononic crystals, Appl. Phys. Lett. **105**, 014107 (2014).

[15] H. Chen, H. K. Zhang, Q. Wu, Y. Huang, H. Nguyen, E. Prodan, X. M. Zhou, and G. L. Huang, Creating synthetic spaces for higher-order topological sound transport, Nat. Commun. **12**, 5028 (2021).

[16] X. C. Xu, Q. Wu, H. Chen, H. Nassar, Y. Y. Chen, A. Norris, M. R. Haberman, and G. L. Huang, Physical Observation of a Robust Acoustic Pumping in Waveguides with Dynamic Boundary, Phys. Rev. Lett. **125**, 253901 (2020).

[17] Z. L. Du, H. Chen, and G. L. Huang, Optimal quantum valley Hall insulators by rationally engineering Berry curvature and band structure, J. Mech. Phys. Solids **135**, 103784 (2020).

[18] H. Chen, H. Nassar, A. N. Norris, and G. L. Huang, Elastic quantum spin Hall effect in kagome lattices, Phys. Rev. B **98**, 094302 (2018).

[19] Y. Chen, Q. Zhang, Y. F. Zhang, B. Z. Xia, X. N. Liu, X. M. Zhou, C. Q. Chen, and G. K. Hu, Research progress of elastic topological materials, Adv. Mech. **51**, 189 (2021).

[20] R. Fleury, D. L. Sounas, C. F. Sieck, M. R. Haberman, and A. Alù, Sound isolation and giant linear nonreciprocity in a compact acoustic circulator, Science **343**, 516 (2014).

[21] X. Ni, C. He, X. C. Sun, X. P. Liu, M. H. Lu, L. Feng, and Y. F. Chen, Topologically protected one-way edge mode in networks of acoustic resonators with circulating air flow, New J. Phys. **17**, 053016 (2015).

[22] Z. J. Yang, F. Gao, X. H. Shi, X. Lin, Z. Gao, Y. D. Chong, and B. L. Zhang, Topological Acoustics, Phys. Rev. Lett. **114**, 114301 (2015).

[23] A. B. Khanikaev, R. Fleury, S. H. Mousavi, and A. Alù, Topologically robust sound propagation in an angular-momentum-biased graphene-like resonator lattice, Nat. Commun. **6**, 8260 (2015).

[24] C. He, X. Ni, H. Ge, X. C. Sun, Y. B. Chen, M. H. Lu, X. P. Liu, and Y. F. Chen, Acoustic topological insulator and robust one-way sound transport, Nat. Phys. **12**, 1124 (2016).

[25] J. Y. Lu, C. Y. Qiu, M. Z. Ke, and Z. Y. Liu, Valley Vortex States in Sonic Crystals, Phys. Rev. Lett. **116**, 093901 (2016).

[26] L. P. Ye, C. Y. Qiu, J. Y. Lu, X. H. Wen, Y. Y. Shen, M. Z. Ke, F. Zhang, and Z. Y. Liu, Observation of acoustic valley vortex states and valley-chirality locked beam splitting, Phys. Rev. B **95**, 174106 (2017).

[27] J. Vila, R. K. Pal, and M. Ruzzene, Observation of topological valley modes in an elastic hexagonal lattice, Phys. Rev. B **96**, 134307 (2017).

[28] T. W. Liu and F. Semperlotti, Tunable Acoustic Valley–Hall Edge States in Reconfigurable Phononic Elastic Waveguides, Phys. Rev. Appl. **9**, 014001 (2018).
[29] Z. Wang, S. Y. Yu, F. K. Liu, Y. Tian, S. K. Gupta, M. H. Lu, and Y. F. Chen, Slow and robust plate acoustic waveguiding with valley-dependent pseudospins, Appl. Phys. Express **11**, 107301 (2018).
[30] N. Gao, S. C. Qu, L. Si, J. Wang, and W. Q. Chen, Broadband topological valley transport of elastic wave in reconfigurable phononic crystal plate, Appl. Phys. Lett. **118**, 063502 (2021).
[31] M. Yan, J. Y. Lu, F. Li, W. Y. Deng, X. Q. Huang, J. H. Ma, and Z. Y. Liu, On-chip valley topological materials for elastic wave manipulation, Nat. Mater. **17**, 993 (2018).
[32] J. J. Chen, S. Y. Huo, Z. G. Geng, H. B. Huang, and X. F. Zhu, Topological valley transport of plate-mode waves in a homogenous thin plate with periodic stubbed surface, AIP Adv. **7**, 115215 (2017).
[33] L. Y. Yang, K. P. Yu, Y. Wu, R. Zhao, and S. S. Liu, Topological spin-Hall edge states of flexural wave in perforated metamaterial plates, J. Phys. D: Appl. Phys. **51**, 325302 (2018).
[34] S. Y. Huo, J. J. Chen, H. B. Huang, and G. L. Huang, Simultaneous multi-band valley protected topological edge states of shear vertical wave in two dimensional phononic crystals with veins, Sci. Rep. **7**, 10335 (2017).
[35] R. Chaunsali, C. W. Chen, and J. Yang, Experimental demonstration of topological waveguiding in elastic plates with local resonators, New J. Phys. **20**, 113036 (2018).
[36] P. Wang, L. Lu, and K. Bertoldi, Topological Phononic Crystals with One-Way Elastic Edge Waves, Phys. Rev. Lett. **115**, 104302 (2015).
[37] R. Zhao, G. D. Xie, M. L. N. Chen, Z. H. Lan, Z. X. H. and W, and E. I. Sha, First-principle calculation of Chern number in gyrotropic photonic crystals, Opt. Express **28**, 4638 (2020).
[38] S. F. Li, I. Kim, S. Iwamoto, J. F. Zang, and J. Yang, Valley anisotropy in elastic metamaterials, Phys. Rev. B **100**, 195102 (2019).
[39] H. Zhu, T. W. Liu, and F. Semperlotti, Design and experimental observation of valley-Hall edge states in diatomic-graphene-like elastic waveguides, Phys. Rev. B **97**, 174301 (2018).
[40] I. Kim, Y. Arakawa, and S. Iwamoto, Design of GaAs-based valley phononic crystals with multiple complete phononic bandgaps at ultrahigh frequency, Appl. Phys. Express **12**, 047001 (2019).
[41] K. Wang, Y. Ren, X. Deng, S. A. Yang, J. Jung, and Z. Qiao, Gate-tunable current partition in graphene-based topological zero lines, Phys. Rev. B **95**, 245420 (2017).
[42] D. P. Morgan, A history of surface acoustic wave devices, Int. J. High Speed Electron. Syst. **10**, 553 (2000).